# Magma-Hydrothermal Interactions at the Costa Rica Rift from Data Collected in 1994 and 2015

R.P. Lowell[1], L. Zhang[3], M.A.M. Maqueda[2], D. Banyte[2], V.C.H. Tong[3], R.E.R. Johnston[5], R.N. Harris[4], R.W. Hobbs[5], C. Peirce[5], A.H. Robinson[5], and K. Kolandaivelu[1]

[1]Department of Geosciences, Virginia Tech, Blacksburg, VA 2406, United States

[2]School of Natural and Environmental Sciences, Newcastle University, Newcastle, NE1 7RU, United Kingdom

[3]Department of Earth Sciences, University College London, United Kingdom

[4]College of Ocean and Atmospheric Sciences, Oregon State University, Corvallis, OR 97331, United States (rharris@ceoas.oregonstate.edu)

[5]Department of Earth Sciences, Durham University, Lower Mountjoy, South Road, Durham, DH1 3LE, United Kingdom.

**Abstract**

We use co-located CTD/transmissometry casts and multichannel seismic reflection surveys conducted at the Costa Rica Rift (CRR) to provide a better understanding of magma-hydrothermal processes occurring at an intermediate-rate spreading center. Water column observations reveal an ~200 m thick plume head ~650 m above the seafloor, which corresponds to a hydrothermal heat output of ~200 ± 100 MW at the ridge axis. Assuming a hydrothermal vent temperature of 350°C and a discharge area between $10^4$ and $10^5$ $m^2$, this heat output implies a mean crustal permeability within the discharge zone of between 2 x $10^{-14}$ and 6 x $10^{-13}$ $m^2$, and a conductive thermal boundary layer thickness of ~20 m. The volume of magma required to maintain the current hydrothermal heat output over the past two decades should result in an across-axis axial magma lens (AML) width between 270 and 1300 m, depending on the amount of cooling and crystallization. However, seismic reflection images, acquired in 1994 and 2015, while showing an apparent along-axis growth of the AML from 2.4 to 6.0 km between surveys, also suggest that, as of 2015, the AML has an apparent across-axis width of no more than 300 m, and that magma delivery at the intermediate spreading rate CRR may be episodic on time scales of tens of years. The data on magma-hydrothermal interactions at the CRR collected in 1994 and 2015 suggest that the hydrothermal system may have significantly cooled and crystallized the AML, primarily in the across-axis direction, and that this hydrothermal system may also episodically turn on and off. The current pattern of microseismicity supports this conclusion, with events not only mirroring the AML depth and location beneath the ridge axis, but also having a temporally varying focus.

## 1. Introduction

An aim of the OSCAR project (O*ceanographic and* S*eismic* C*haracterization of heat dissipation and alteration by hydrothermal fluids at an* A*xial* R*idge*) was to develop a basin-scale model of deep ocean circulation. To this end, a large-scale interdisciplinary geophysical and oceanographic exploration of the Panama Basin, in the eastern Pacific, was conducted between December 2014 and March 2015. A key part of this program focused on the east-west trending, intermediate spreading rate Costa Rica Rift (CRR) (Figure 1), which runs from 3°20′N, 84°11′W to 3°19′N, 83°15′W and is characterized by a 103 km-long rift valley bounded by the Ecuador Fracture Zone to the west and the Panama Fracture Zone to the east. The CRR is asymmetrically spreading with a half rate of 20-25 mm $yr^{-1}$ to the north (the Cocos Plate) and 35-40 mm $yr^{-1}$ to the south (the Nazca Plate) [*Wilson et al.*, 2019]. At 3°20′N, 83°44′W, the ridge is divided into two second-order segments by a small non-transform discontinuity (NTD), where the two segment tips overlap by 2.4 km and are offset by ~1.5 km laterally.

In 1994, RV Maurice Ewing cruise EW9416 imaged a seismic reflector (~2.8 km depth) beneath the bathymetrically shallowest seafloor at the ridge axis (~2900 m below sea level) approximately ~10 km west of the NTD [*Buck et al.*, 1997; *Floyd et al.*, 2002]. In common with seismic reflection studies at other oceanic spreading centers over a range of spreading rates [e.g., *Detrick et al.*, 1987; *Navin et al.,* 1998; *Canales et al.*, 2006; *Singh et al.*, 2006; *Jacobs et al.*, 2007; *Van Ark et al.*, 2007; *Carbotte et al.*, 2013] this reflector was interpreted as evidence of an axial magma lens (AML). As such, this location offered an ideal target to investigate the

relationship between crustal heat flow, heat output to the water column, the nature of the heat source and how hydrothermal fluid flow is sustained.

Consequently, during OSCAR cruise RRS James Cook JC112/113, a number of conductivity, temperature and transmissometry versus depth measurements (henceforth referred to as CTTD data) were made in the water column above the location of the EW9416 seismic line and in the vicinity of the CRR axis [*Banyte et al.*, 2018]. The goal of the CTTD casts was to determine whether there was evidence of current hydrothermal activity in the water column at the ridge axis. Water samples were also collected to determine the $^{3}$He distribution in the water column, in order to characterize and determine the distribution of any hydrothermal emissions.

In addition, the 1994 multichannel seismic (MCS) survey was also repeated during OSCAR cruise RRS James Cook JC114 [*Hobbs and Peirce*, 2015] to appraise the AML's temporal characteristics and to better constrain its dimensions and extent along-axis. As part of this survey a 3D grid of ocean-bottom seismographs (OBSs) was also deployed across the CRR to provide a ridge-axis velocity model to enable depth conversion [*Zhang et al.,* 2016; 2017]. A vertical array of hydrophones recorded the down-going seismic waveform to enable source signature matching to the 1994 data. MCS lines perpendicular to the ridge axis were also acquired during JC114 to determine the across axis width of the AML (Figure 1); and a transect to the ODP 504B borehole was acquired to provide geophysical versus geological ground truth [*Wilson et al.*, 2019].

In this paper, we describe the results of co-located water column measurements and seismic reflection images acquired at the CRR, and provide new insights into the coupled magma-

hydrothermal interactions at this intermediate spreading ridge system (Figure 2). We apply buoyant plume theory to estimate the heat output of the hydrothermal plume, and use the single pass model [e.g., *Lowell and Germanovich*, 2004; *Lowell et al.*, 2013] to estimate the mass flow rate and crustal permeability at the CRR axis. By combining our heat output estimates with the observed dimensions and extent of the AML in 1994 and 2015, we appraise the role played by the AML in driving hydrothermal circulation. Finally, we speculate on the nature and longevity of hydrothermal fluid flow at the CRR.

## 2. Oceanographic observations of the hydrothermal system

Transmissometry data from seven CTTD casts at and near the axis of the CRR (Figure 3a) indicate that there is a measurable decrease in beam transmission over a 200 m-deep zone with its top located ~650 m above the 3150 m-deep seafloor. We interpret this decrease in beam transmission as resulting from a higher concentration of particulate matter within this zone, indicative of a hydrothermal plume reaching neutral buoyancy at this height above seafloor [e.g., *Baker et al.*, 1985; *Baker and Massoth*, 1987]. Evidence for the presence of hydrothermal activity is also provided by helium isotope data at ocean ridges [e.g., *Lupton*, 1998]. Here the data show an ~50% increase in $^{3}He$ concentration at an equivalent depth, compared to background values in the surrounding area (Figure 3b).

As a hot hydrothermal plume buoyantly ascends from the seafloor it entrains surrounding seawater. As a result of fluid phase separation in the sub-seafloor, the salinity of plume water may be different to that of seawater. The ascending mixture of hydrothermal plume fluid and

entrained seawater will gradually reach a level of neutral buoyancy and will then spread laterally [e.g., *Turner and Campbell*, 1987]. The maximum rise height of the plume is a function of the buoyancy flux and the density structure of the ocean above, which is described by the Brunt-Väisälä, or buoyancy, frequency $N$. The Brunt–Väisälä frequency is defined as $N = \sqrt{-g\,\rho_z/\rho}$, where $g$ is the acceleration due to gravity, $\rho$ is potential density, and $\rho_z$ denotes the partial derivative of $\rho$ with respect to the vertical coordinate, $z$. We calculate $\rho$ from the CTTD potential temperature, conductivity/salinity and pressure data using the Thermodynamic Equation of Seawater -2010 (TEOS-10) formulation [*IOC et al.*, 2010]. From the maximum rise height of the plume $Z^*$ can be expressed by [*Turner and Campbell*, 1987],

$$Z^* = 3.8 F_0^{1/4} N^{-3/4}, \quad (1)$$

where the numerical factor 3.8 represents an average rate of entrainment over the height of the plume as derived from a number of laboratory experiments [*Turner*, 1986]. The buoyancy flux $F_0$ is defined as,

$$F_0 = Q\frac{\Delta\rho}{\rho_0}g, \quad (2)$$

where $Q$ is the volume flow rate in $m^3\ s^{-1}$ and $\Delta\rho$ is the density difference between hydrothermal fluid and seawater. Symbols and parameter values are given in Table 1. Although $\Delta\rho/\rho_0$ may result from both salinity and temperature differences, here we assume that the primary factor is the difference in temperature. Hence,

$\Delta\rho/\rho_0 = \alpha\Delta T$,

where $\alpha$ is the thermal expansion coefficient of seawater. Given that the heat output, $H$, in the hydrothermal plume is,

$$H = \rho c_p Q \Delta T \,, \tag{3}$$

where $c_p$ is the specific heat at constant pressure, the heat output can then be written in terms of the buoyancy flux $F_0$ or the maximum plume rise height, $Z^*$, as

$$H = \frac{\rho c_p}{\alpha g} F_0 = \frac{\rho c_p}{\alpha g}\left(\frac{Z^*}{3.8}\right)^4 N^3 . \tag{4}$$

The strong dependence of $H$ on $Z^*$ and $N$ suggests that small errors in these parameters can lead to significant errors in the estimated value of $H$.

Figure 3c shows the abyssal density stratification, $N^2$, determined from the CTTD casts undertaken at the CRR axis, plotted with depth. The graph shows that $N^2$ gradually increases with height above seabed, with a sharp change in gradient near 2500 m depth. This depth, which coincides with the top of the zone of decreased transmissivity and interpreted as the top of a hydrothermal plume head (Figure 3a), likely results from a change in ocean dynamics at depths less than 2500 m. The average value of $N^2$ between 3150 m and 2500 m depth is ~2 x $10^{-7}$ $s^{-2}$.

Using parameter values from Table 1, a maximum rise height for the plume, and a $Z^*$ of ~650 m, we obtain a heat output, $H$, of ~200 ± 100 MW. Uncertainties in H stem from uncertainties in Z* (±10 m), $N^2$ (±0.5 x 10-7 $s^{-2}$), and the average value of $N^2$ at the relevant depth of 0.25 x $10^{-6}$ $s^{-2}$ (Figure 3c). This heat output is similar to estimates for hydrothermal systems at other mid-ocean ridges [e.g., *Baker*, 2007], and suggests that the observed CRR plume likely results from a high-temperature black smoker-like system. Data from seafloor hydrothermal systems indicate that although most of the heat output occurs in the form of diffuse flow, 80-90% of hydrothermal heat output is derived from high-temperature magma driven flow [Mittlelstaedt et al., 2012; Lowell et al., 2013].

Although direct measurements of the hydrothermal vent temperature at the CRR are not available, black smoker temperatures are typically ~350°C [e.g., *Lowell et al.*, 2013]. Using a $\Delta T$ value of 350°C, equation (3) yields a volumetric flow rate of $0.1 \leq Q \leq 0.2$ $m^3$ $s^{-1}$. Assuming that this flow is driven by buoyancy differences between cold recharge fluid and hot vent fluid within the permeable crust, an integrated expression of Darcy's Law (assuming that the main resistance to hydrothermal flow occurs in the discharge zone) enables an estimate of crustal permeability to be made using,

$$Q = \frac{\alpha_d g k_d T_v A_d}{\nu_d}, \qquad (5)$$

where $k_d$ is the permeability, $T_v$ is the mean vent temperature, $A_d$ is the area of the discharge zone, and $v_d$ is the kinematic viscosity. The subscript $d$ is used to indicate properties of the discharge zone.

Substituting the above values for $Q$ into equation (5) together with the parameter values from Table 1, we obtain $2 \times 10^{-9} \leq k_d A_d \leq 6 \times 10^{-9}$ m$^4$. Given that the footprint areas of vent fields are typically observed to lie between $10^4$ and $10^5$ m$^2$ [e.g., *Lowell et al.*, 2013], we estimate that the crustal permeability in the CRR hydrothermal discharge region lies between $2 \times 10^{-14}$ and $6 \times 10^{-13}$ m$^2$, similar to that estimated for many seafloor systems [*Lowell et al.*, 2013].

Having determined the amount of heat being output into the water column at the CRR, we can now use this estimate to provide an insight into the nature of the heat source, by determining the extent and temporal characteristics of the axial magmatic system as evidenced by the observed AML.

## 3. Seismic observations of the AML

To enable direct comparison of the 1994 [along-axis line 1268 (EW9416)] and 2015 [along-axis line NG_Bb13 and across-axis line NG_G10 (JC114)] MCS lines, all lines have been processed in an identical manner to final migrated form [*Zhang et al.,* 2017]. Details of the acquisition can be found in the JC114 cruise report [*Hobbs and Peirce*, 2015] and the processing sequence included: trace editing, divergence correction and amplitude balancing, band-pass filtering, Kirchhoff pre-stack time migration, muting, stacking, and noise suppression. To maintain

196 consistency in data processing between surveys, the pre-stack time migration of both along-axis
197 lines was applied with the same velocity model, which was based on the velocity analysis of line
198 1268, and waveform matching between the 1994 and 2015 surveys was applied based on the
199 vertical hydrophone recording of the down-going waveform during JC114. MCS image depth
200 conversion was undertaken using a sub-seabed velocity structure and was derived from modeling of
201 OBS and MCS gather travel-time picks [*Wilson et al.*, 2019; *Robinson et al.*, in revision].
202
203 Both MCS surveys image an AML at approximately the same two-way travel time (TWTT) sub-
204 seabed (Figure 4). The reprocessed line 1268 from the original 1994 survey (Figure 4a), shows a
205 2.4 km-long reflection event at 5.1 to 5.3 s two-way travel time (TWTT). The 2.38 km $s^{-1}$
206 stacking velocity of this event precludes it from being a water-path scattered event or a sea
207 surface/water bottom multiple. Modeling of the near-offset traces in the unstacked gathers
208 (Figure 5) shows that the reflection event corresponds to a thin, low velocity anomaly, where the
209 velocity may be as low as 4.5 km $s^{-1}$, and where its thickness may be of the order of ~100 m.
210 Using the background upper crustal velocity model, the AML imaged in 1994 has an apparent
211 eastward dip, lying between 3.0-3.5 km below the seafloor.
212
213 Line NG_Bb13, from the more recent 2015 resurvey, was navigated to the location of line 1268
214 to better than the Fresnel radius of ~500 m at AML depth, assuming a dominant frequency of 20
215 Hz. This line (Figure 4b) also images the AML reflection at 5.1 to 5.3 s TWTT (3.0-3.5 km
216 below the seafloor), suggesting a consistency of melt supply to the ridge-axis with at least an
217 ~20-year episodicity, that also arrives at 5.1 to 5.3 s TWTT (3.0-3.5 km below the seafloor). This
218 reflection event has a total length of ~6 km, where the additional length results from an extension

219 westward from the AML as originally imaged in 1994. Along-axis variation in reflection true
220 amplitude suggests that, as of 2015, the AML may possibly be split into two limbs, with a gap of
221 ~600 m between them (Figure 4b). The eastern limb effectively mirrors that of line 1268, but
222 extends westward for ~650 m, whereas the western limb, which is only observed on line
223 NG_Bb13, extends the AML an additional 2.5 km.
224
225 AMLs detected along the intermediate spreading Juan de Fuca Ridge [*Van Ark et al.*, 2007] and
226 the fast spreading East Pacific Rise [*Carbotte et al.*, 2013], typically have an across-axis width of
227 between ~500 and 1000 m. However, the orthogonal line NG_G10 (Figure 4c) from the 2015
228 survey does not show a similar expression of an AML reflection event. This observation at the
229 CRR may indicate that the width of the AML is similar to the lateral resolution of the seismic
230 signal which, for the 20 Hz peak frequency, suggests a width of no more than ~60 m. The line
231 NG_G10 image possibly shows a narrow-width event whose diffraction would intersect line
232 NG_Bb13 at the time of the imaged AML reflection. The event is no more than 300 m wide,
233 which we assume as an estimate for the maximum-width case analyzed below. The apparently
234 narrow width of the AML at the CRR could possibly indicate enhanced lateral hydrothermal
235 circulation that rapidly freezes the melt lens in both off-axis directions. Based on the above we
236 estimate the areal extent of the AML, as of 2015, to be less than ~1.8 x $10^6$ $m^2$.
237
238 **4. Link between AML and hydrothermal heat output**
239
240 Using the estimated heat output at the CRR of ~200 MW and an estimated magma heat transfer
241 area ($A_m$) of 1.8 x $10^6$ $m^2$, we construct a simple heat balance model for heat transfer from the

AML to the hydrothermal system. We assume conduction across a thermal boundary layer of thickness, $\delta$, following *Lowell and Germanovich* [2004] and *Lowell et al.* [2013],

$$H = \frac{\lambda(T_m - T_v/2)A_m}{\delta}, \quad (6)$$

where $\lambda$ is the thermal conductivity of the host rock, and $T_m$ is the mean temperature of the AML. Using parameters defined in Table 1, and the subscript $m$ to indicate properties of the magma, we obtain a thermal boundary layer of thickness of ~20 m, similar to estimates for other ridge axis systems [*Lowell et al.*, 2013] and ophiolites and tectonic windows [e.g., *Gillis*, 2008]. Our estimated uncertainty in $\delta$ is ± 10 m primarily based on the uncertainty in H and we note that the thermal boundary layer thickness scales linearly with $A_m$, so a smaller $A_m$ would yield a smaller $\delta$.

However, to maintain the estimated heat output in a quasi-steady-state, this thermal boundary layer must retain an effectively constant thickness [*Lowell and Germanovich*, 2004] which, in turn, necessitates the influx of fresh magma into the AML [*Liu and Lowell*, 2009; *Choi and Lowell*, 2015]. Following *Lowell et al.* [2013] we assume that the observed hydrothermal heat output is driven by heat transfer from the magma that has replenished the AML, cooled and partially crystalized between 1994 and 2015. The mean rate of magma replenishment, $dV_m/dt$, needed to maintain a hydrothermal heat output can be written as,

$$H = (\rho_m c_m \Delta T + \rho_m \chi L)(dV_m/dt), \quad (7)$$

where $\chi$ is the crystal fraction, and the first term in parenthesis on the right side of equation (7) is the sum of the sensible and latent heat released as the melt cools and crystallizes. Although the MCS data do not provide direct information regarding the state of the AML volume, internal temperature and crystal content, the images do show that the AML still exists where it was first imaged in 1994, and further show that it has apparently doubled in length, largely westwards. Hence the MCS data suggest magma replenishment and AML growth between 1994 and 2015, either constantly or episodically, since in this time frame the AML imaged in 1994 would otherwise have solidified, and hydrothermal heat output that may have been present in 1994 would have declined. Without magma replenishment, crystal suspended simulations of AML cooling show a rapid decrease in heat output and hydrothermal temperature such that crystallinity reaches 60% in less than 10 years [*Liu and Lowell*, 2009].

Although mid-ocean ridge magma supply shows variability on decadal time scales, we start by estimating the mean rate of magma replenishment required to maintain the hydrothermal system at a quasi-steady-state heat output of 200 MW for the past two decades. We assume quasi-steady-state input magma at its liquidus temperature. For simplicity, we further assume that each initial cooling of 10°C leads to 5% fractional crystallization [*Maclennan*, 2008; *Lowell et al*., 2013]. If magmatic heat transfer is accompanied by cooling of 20°C, as observed at 9°50′N at the East Pacific Rise between the eruptions of 1991/1992 and 2005/2006 [*Goss et al.,* 2010], the heat released by cooling of the replenished magma is ~60 MJ $m^{-3}$ + ~110 MJ $m^{-3}$, corresponding to the sensible and latent heat respectively, or ~170 MJ $m^{-3}$ in total. Substituting this value of heat release into equation (7) yields a magma replenishment rate, $dV_m/dt$, *of* ~1.2 $m^3$ $s^{-1}$. With these

assumptions and values the amount of magma replenishment between 1994 and 2015 would be ~7.8 x $10^8$ $m^3$. Given that the maximum vertical cross-sectional area of the AML is ~6 x $10^3$ m-long x 100 m-deep, the amount of magma needed to sustain the hydrothermal system would extend ~1300 m across-axis, more than four times the upper estimate of ~300 m suggested by the 2015 MCS data images, and well within the navigational precision of both the 1994 and 2015 surveys. If cooling and/or crystallization is greater as might be expected from hydrothermal circulation a smaller magma replenishment rate is possible. For example, if the amount of magma cooling is 100°C, with 50% crystallization, the resulting rate of magma replenishment needed to sustain the 200 MW hydrothermal system would be 0.24 $m^3$ $s^{-1}$ and the volume of magma emplaced would be 1.6 x $10^8$ $m^3$. In this scenario the expected across-axis width of the AML would be ~270 m, which is of the same order as the putative AML width.

It is also possible, however, that magma replenishment is episodic even on a 20-year time scale and that hydrothermal heat output would then wax and wane in that time frame. Finite width dikes in layer 2B suggest discrete intrusion events every 10-100 years [*Head et al.*, 1996]. At an intermediate spreading center such as the CRR magma replenishment is likely to be more infrequent than at the fast spreading East Pacific Rise over long time scales. If the plume represented the heat from a single replenishment event, the volume of magma needed to generate the 200 MW of heat would scale with time since the event.

## 5. Discussion

309 CTTD data indicates the presence of a hydrothermal plume above the CRR, that has a heat
310 output of ~200 ±100 MW. MCS images have enabled estimation of AML dimensions and
311 magma replenishment characteristics at the CRR. Our modeling results assume quasi-steady state
312 behavior. However, the MCS data may, instead, be suggesting episodic AML replenishment. The
313 contrasting pattern of AML reflectivity between the 1994 and 2015 surveys (Figure 4) suggests
314 that the western region of the ridge axis is the current focus of magma replenishment, and that it
315 could possibly be disconnected from the eastern limb as a result of rapid, focused, hydrothermal
316 cooling. Alternatively, the two limbs may be joined, supplied via a single magma source, with
317 the apparent gap between the western and eastern limbs an artifact of out-of-plane interference
318 and scattering of seismic energy by the rugged seafloor topography above. The lack of a clear
319 across-axis reflection event from the AML suggests a narrow width perpendicular to the
320 spreading direction, whereby the AML appears to be a ribbon of magma extending ~6 km along
321 the ridge axis with a maximum width of 300 m, significantly narrower than AMLs observed at
322 other intermediate [e.g., *Van Ark et al.*, 2007] or the faster spreading ridges [e.g., *Kent et al.*,
323 1993].
324
325 The extent of the AML along axis suggests significant westward magma replenishment has
326 occurred, raising the question of whether the inferred volume of magma replenishment required
327 to maintain a 200 MW hydrothermal system can do so for two decades, or instead if the
328 replenishment process is more likely to be episodic. Assuming that magma is added to the AML
329 over its entire current length of ~6 km, we find that to maintain a 200 MW hydrothermal system
330 for 20 years, the across-axis width of the AML would have to range between ~270 and 1300 m,
331 depending on the degree of cooling and crystallization assumed. Given the estimated AML

width, it is possible that either the observed hydrothermal heat output is a result of significant/enhanced cooling of a consistent magma replenishment, or a result of more recent replenishment focused towards the western end of the ridge axis. Numerical models of two-phase flow in NaCl-$H_2O$ systems indicate that there is a lag time of years to decades between the decay of heat input at the base of the system and changes in seafloor vent temperatures and heat output [*Singh et al.*, 2013; *Choi and Lowell*, 2015]. Consequently, the currently observed heat output may reflect an episode of magma replenishment in the recent past (years to decades), and the westward extending AML reflectivity suggests, in turn, an apparently thin ribbon of recent magma replenishment into the AML that has yet to spread in the across axis direction.

A new episode of magma input, associated with a phase of diking, may generate an event plume [e.g., *Baker et al.*, 1987, 1998; *Lowell and Germanovich*, 1995]. In this case, the heat output and $^3$He anomaly recorded in the observed water column plume may reflect a transient event rather than be an indication of quasi-steady-state hydrothermal heat flux. A repeat CTTD survey conducted two weeks later in the same area (Figure 3b) failed to detect the plume which may support a transitory cause or, more simply, a change in ocean currents or tidal flows may have displaced it from its previously observed location.

One hundred and sixteen of the more significant microearthquakes recorded during the 2015 OBS survey were hand-picked, and their hypocenters projected onto a depth-converted migrated image of line NG_Bb13 (Figure 6). These locations were estimated using the NonLinLoc software (*Lomax et al.*, 2000) based on a 1D crustal velocity model derived from modeling of both OBS and MCS gather travel time picks [*Wilson et al.,* 2019; *Robinson et al.,* in revision].

355 This analysis shows that the majority of these events recorded during a 21-day period are
356 distributed at or above the AML between 83º48′W and 83º52′W. Analyzing the distribution of
357 seismicity suggests that there are two principal event populations. The initial cluster of
358 seismicity, between Julian days (JD) 26-34, is located above and to the east of the gap between
359 the two AML limbs, and extends from AML depth to the seabed. It is not clear whether there is a
360 discernible migration in the depth of seismicity, either upward or downward, over the period of
361 this cluster. However, similar observations elsewhere [e.g., *Tolstoy et al.* 2008; *Dziak et al.*,
362 2007] correlate such seismicity with the existence of active, high-temperature hydrothermal
363 circulation within the upper crust that would transfer heat from the underlying AML. This
364 correlation between heat source and seismicity may, therefore, reflect hydraulic fracturing within
365 the hydrothermal circulation system [e.g., Wilcock et al., 2009]. Further, *Fontaine et al.* [2011]
366 predict that localized hydrothermal cells will cause along strike variation in the size of an AML
367 on a scale-length of hundreds of meters, so our estimate of the AML width under the CRR, based
368 on a single MCS line, even though repeated, is open to debate. Possible evidence for this
369 interaction is provided by the second cluster, between JD 35-47, which predominantly occurs
370 above the western AML limb and is confined to depths >5 km, suggesting that this population
371 may be related to changes in the AML volume. The apparent lack of seismicity between the
372 AML and the NTD may also suggest the presence of a cooling front, limiting eastward melt
373 migration.
374
375 Although our analysis of magma-hydrothermal interactions at the CRR suggests that magma
376 supply may be episodic even on a decadal scale, episodic magma supply likely occurs over much
377 longer time scales as well. Hence the ridge axis may, therefore, evolve through alternating

phases of tectonism and magmatic accretion [*Kappel and Ryan*, 1986]. This interpretation is supported by off-axis observations at the CRR [*Wilson et al*., 2019] which demonstrate the variable crustal formation modes that have occurred at this ridge system over 7 Ma. We suggest, therefore, that intermediate spreading ridge systems may represent a finely balanced environment, where changes in the rates of magma supply, tectonic extension, and hydrothermal cooling may shift the equilibrium state towards different end-member spreading modes.

## 6. Conclusions

The combination of water column data and repeat multichannel seismic surveys at the CRR axis enables us to make a preliminary appraisal of magma-hydrothermal interactions at this intermediate spreading ridge. The results suggest that current hydrothermal heat output at the CRR may be the result of continuous or episodic magma replenishment, that has undergone significant cooling by hydrothermal circulation. Alternatively, the observed hydrothermal plume may represent a transient event such as an event plume associated with a recent input of magma into the AML coupled with a phase of diking. In either case, the MCS data clearly show both temporal and spatial changes in AML characteristics at the CRR axis on a decadal time scale, and these changes may be reflected in corresponding changes in hydrothermal discharge. Additional information on the state of the CRR hydrothermal system is required to determine whether it is in a decaying or a growing phase, which can only be gleaned from a detailed seafloor morphological and sampling study, supported by a high-resolution 3D volume seismic survey to correctly map the location of the AML both along and across the ridge axis.

**Acknowledgements**

This research project was funded by the National Science Foundation grants OCE 1353114 and 1558797 to RPL, NSF grants OCE 1353003 and 1558824 to RNH, and by the Natural Environmental Research Council (NERC) grants NE/I027010/1 to Durham University (RWH and CP), NE/I022868/1 and NE/I022868/2 to the University of Newcastle (MAAM), and (NE/1022957) to University College, London (VCHT). We would like to thank all those involved in the planning and acquisition of data during research cruises JC112/3 and JC114, including the officers, engineers and crew of the RRS James Cook, the scientific party, and all seagoing NERC facility technicians and engineers. The MCS data were processed using GLOBE Claritas[TM], and manipulated for plotting using Seismic Unix. The MCS source characteristics were recorded by the NERC Ocean-Bottom Instrumentation Facility (*Minshull et al*., 2005). Figures were prepared using the Generic Mapping Tools (GMT). Data from JC112/3 and JC114 are archived at the NERC's British Oceanographic Data Center and at Durham University, and are available on request. Two anonymous reviewers helped us improve the clarity of this paper. Sadly, Bob Lowell passed away while this, his last paper, was in review. Throughout his long career, Bob made major contributions to our understanding of the thermal and fluid dynamics of hydrothermal systems and the characteristics of their magma-source drivers. In this OSCAR project, we greatly benefited from that wealth of knowledge and, in particular, his geological insights into the interpretation of the geophysical and oceanographic imaging. The final accepted version of this manuscript is available through Durham Research Online (dro.dur.ac.uk).

## References


Baker, E.T. (2007), Hydrothermal cooling of Mid-Ocean Ridge axes: Do measured and modeled heat fluxes agree?, *Earth Planet. Sci. Lett., 263*, 140-150, doi:10.1016/j.epsl.2007.09.010.

Baker, E.T. and G.J. Massoth (1987), Characteristics of hydrothermal plumes from two vent fields on the Juan de Fuca Ridge, northeast Pacific Ocean, *Earth Planet. Sci. Lett.*, *85*, 59-73, doi:10.1016/0012-821X(87)90021-5.

Baker, E.T., J.W. Lavelle and G.J. Massoth (1985), Hydrothermal particle plumes over the southern Juan de Fuca Ridge, *Nature*, *316*, 342-344.

Baker, E.T., G.J. Massoth and R.A. Feely (1987), Cataclysmic hydrothermal venting on the Juan de Fuca Ridge, *Nature*, *329*, 149-151.

Baker, E.T., G.J. Massoth, R.A. Feely, G.A. Cannon and R.E. Thomson (1998), The rise and fall of the CoAxial hydrothermal site, 1993-1996, *J. Geophys. Res., 103*, 9791-9806, doi:10.1029/97JB03112.

Banyte D, M.A. Morales Maqueda, D.A. Smeed, R. Hobbs, A. Megann, and S. Recalde (2018), Geothermal heating in the Panama Basin: 1. Hydrography of the Basin. *J. Geophys. Res. Oceans*, *123*, 7382-7392, doi:10.1029/2018JC13868.

446 Buck, W.R., S.M. Carbotte and C. Mutter (1997), Controls on extrusion at mid-ocean ridges,
447 *Geology*, *25*, 935-938, doi:10.1130/0091-7613(1997)025<0935:COEAMO>2.3.CO;2.
448
449 Canales, J.P., S.C. Singh, R.S. Detrick, S.M. Carbotte, A. Harding, G.M. Kent, J.B. Diebold, J.
450 Babcock and M.R. Nedimovic (2006), Seismic evidence for variations in axial magma
451 chamber properties along the southern Juan de Fuca Ridge, *Earth Planet. Sci. Lett*., *246*,
452 353-366, doi:10.1016/j.epsl.2006.04.032.
453
454 Carbotte, S.M., M. Marjanovic, H. Carton, J.C. Mutter, J.P. Canales, M.R. Nedimovic, S. Han
455 and M.R. Perfit (2013), Fine-scale segmentation of the crustal magma reservoir beneath the
456 East Pacific Rise, *Nature Geosci*., doi:10.1038/NGEO1933.
457
458 Choi, J. and R.P. Lowell (2015), The response of two-phase hydrothermal systems to changing
459 magmatic heat input at mid-ocean ridges, *Deep Sea Res II*, *121*, 17-30,
460 doi:10.1016/j.dsr2.2015.05.005.
461
462 Detrick, R.S., P. Buhl, E. Vera, J. Mutter, J. Orcutt, J. Madsen and T. Brocher (1987), Multi-
463 channel seismic imaging of a crustal magma chamber along the East Pacific Rise, *Nature*,
464 *326*, 35-41.
465
466 Dziak, R.P., D.R. Bohnenstiehl, J.P. Cowen, E.T. Baker, K.H. Rubin, J.H. Haxel and M.J.
467 Fowler (2007), Rapid dike emplacement leads to eruptions and hydrothermal plume release
468 during seafloor spreading events, *Geology*, *35*, 579-582, doi:10.1130/G23476A.1.

469

470 Floyd, J.S., J.C. Mutter and S.M. Carbotte. (2002), Seismic reflection imaging of the evolution of
471 ocean crustal structure at the intermediate rate spreading Costa Rica Rift, *EOS Trans. AGU*,
472 *83*, Fall Meeting Suppl., Abstract T12-1318.

473

474 Fontaine, F.J., J.-A. Olive,M. Cannat, J. Escartin and T. Perol (2011), Hydrothermally-induced
475 melt lens cooling and segmentation along the axis of fast-and intermediate-spreading
476 centers, *Geophys. Res. Lett., 38*, L14307, doi:10.1029/2011GL047798.

477

478 Gillis, K.M., (2008), The roof of an axial magma chamber: A hornfelsic heat exchanger,
479 *Geology*, *36*, 292-302, doi:10.1130/G24590A.1.

480

481 GLOBE Claritas Software Documenation 6.0.1 (2012), Institute of Geological and Nuclear
482 Sciences, Ltd.

483

484 Goss, A.R., M.R. Perfit, W.I. Ridley, K.H. Rubin, G.D. Kamenow, S.A. Soule, A. Fundis and
485 D.J. Fornari (2010), Geochemistry of lavas from the 2005-2006 eruption at the
486 East Pacific Rise, 9°46′-9°56′N: Implications for ridge crest plumbing and decadal changes
487 in magma chamber composition, *Geochem. Geophys. Geosyst.*, *11*, Q05T09
488 doi:10.1029/2009GC02977.

489

490 Head, J. W.III, L. Wilson and D.K. Smith (1996), Mid-ocean ridge eruptive vent morphology
491 and substructure, *J. Geophys. Res.*, *101*, 28,265–28,280, doi:10.1029/96JB02275.

Hobbs, R.W. and C. Peirce (2015), RRS James Cook JC114 cruise report, 74pp.

IOC, SCOR and IAPSO (2010), The international thermodynamic equation of seawater – 2010: Calculation and use of thermodynamic properties, Intergovernmental Oceanographic Commission, Manuals and Guides No. 56, UNESCO (English), 196 pp.

Jacobs, A.M., A.J. Harding and G.M. Kent (2007), Axial structure of the Lau back-arc basin from velocity modeling of multichannel seismic data, *Earth Planet. Sci. Lett.*, *259*, 239-255, doi:10.1016/j.epsl.2007.04.021.

Kappel, E.S. and W.B.F Ryan (1986), Volcanic episodicity and a non-steady-state rift valley along northeast Pacific spreading centers: Evidence from SeaMARC I, *J. Geophys. Res.*, *91*(3), 13925–13940, doi:10.1029/JB091iB14p13925.

Kent, G.M., A.J. Harding and J.A. Orcutt (1993), Distribution of magma beneath the East Pacific Rise between the Clipperton Transform and the 9°17′ N deval from forward modelling of common depth point data, *J. Geophys. Res.*, *98*, 13,945-13,969, doi:10.1029/93JB00705.

Liu, L. and R.P. Lowell (2009), Models of hydrothermal heat output from a convecting, crystallizing, replenished magma chamber beneath an oceanic spreading center, *J. Geophys. Res.*, *114*, B02102, doi:10.1029/2008JB005846.

515 Lomax, A., J. Virieux, P. Volant and C. Berge-Thierry (2000), Probabilistic earthquake location
516 in 3D and layered models: Introduction of a Metropolis-Gibbs method and comparison with
517 linear locations, In: *Advances in seismic event location*, edited by C.H. Thurber and N.
518 Rabinowitz, Kluwer, Dordrecht, 101-134, doi:10.1007/978-94-015-9536-0_5.
519
520 Lowell, R.P. and L.N. Germanovich (1995), Dike injection and the formation of megaplumes
521 at ocean ridges, *Science*, *267*, 1804-1807, doi:10.1126/science.267.5205.1804.
522
523 Lowell, R.P. and L.N. Germanovich (2004), Seafloor hydrothermal processes: Results from scale
524 analysis and single-pass models, in *Mid-Ocean Ridges: Hydrothermal Interactions Between*
525 *the Lithosphere and Oceans, Geophys. Monogr. Ser.,* vol. 148, ed. by C.R. German, J. Lin,
526 and L.M. Parson, pp. 219-244, AGU, Washington, D.C.
527
528 Lowell, R.P., A. Farough, J. Hoover and K.C. Cummings (2013), Characteristics of magma-
529 driven hydrothermal systems at oceanic spreading centers, *Geochem. Geophys. Geosyst.*, *14*,
530 1756-1770, doi:10.1002/ggge.20109.
531
532 Lupton, J. (1998), Hydrothermal helium plumes in the Pacific Ocean, *J. Geophys. Res*., *103*,
533 15,853–15,868, doi:10.1029/98JC00146.
534
535 Maclennan, J. (2008), The supply of heat to mid-ocean ridges by crystallization and cooling of
536 mantle melts, in Magma to Microbe: Modeling Hydrothermal Processes at Ocean Spreading
537 Centers, *Geophys. Monogr. Ser., vol. 178*, edited by R. P. Lowell, J. S. Seewald, A.

538 Metaxas, and M.R. Perfit, 285 pp., AGU, Washington D. C., doi:10.1029/GM178.
539
540 Mittelstaedt, E., J. Escartin, N. Gracias, J.-A. Olive, T. Barreyre, A. Davaille, M. Cannat, R.
541 Garcia (2012), Quantifying diffuse and discrete venting at the Tour Eiffel vent site, Lucky
542 Strike hydrothermal field, *Geochem. Geophys. Geosys., 13*, Q04008,
543 doi:10.1029/2011GC003991.
544
545 Minshull, T.A., M.C. Sinha and C. Peirce (2005). Multi-disciplinary, sub-seabed geophysical
546 imaging: a new pool of 28 seafloor instruments in use by the United Kingdom Ocean
547 Bottom Instrument Consortium. *Sea Technology*, *46*(10), 27-31.
548
549 Navin, D.A., C. Peirce and M.C. Sinha, (1998), The RAMESSES experiment - II - Evidence for
550 accumulated melt beneath a slow-spreading ridge from wide-angle refraction and
551 multichannel reflection profiles. *Geophys. J. Int.*, *135* (3), 746-772, doi:10.1046/j.1365-
552 246X.1998.00709.x.
553
554 Singh, S.C., W.C. Crawford, H. Carton, T. Seher, V. Combier, M. Cannat, J.P. Canales, D.
555 Dusunur, J. Escartín and J.M. Miranda (2006), Discovery of a magma chamber and faults
556 beneath a Mid-Atlantic Ridge hydrothermal field, *Nature*, *442*, 1029–1032,
557 doi:10.1038/nature05105.
558

559 Singh, S., R.P. Lowell and K.C. Lewis (2013), Numerical modeling of phase separation at the
560 Main Endeavour Field, Juan de Fuca Ridge, *Geochem. Geophys. Geosyst.*, *14*, 4021-4034,
561 doi:10.1002/ggge.20249.
562
563 Stockwell, J.W. (1999), The CWP/SU: Seismic un*x package, *Computers and Geosciences*, *25*,
564 415-419, doi:10.1016/S0098-3004(98)00145-9.
565
566 Tolstoy, M., F. Waldhauser, D.R. Bohnenstiehl, R.T. Weekly and W.-Y. Kim (2008), Seismic
567 identification of along-axis hydrothermal flow on the East Pacific Rise, *Nature*, *451*,
568 doi:10.1038/nature06424.
569
570 Turner, J.S. (1986), Turbulent entrainment: the development of the entrainment assumption
571 and its application to geophysical flows, *J. Fluid Mech.*, *173*, 431-471,
572 doi:10.1017/S0022112086001222.
573
574 Turner, J.S. and I.H. Campbell (1987), Temperature, density and buoyancy flux in "black
575 smoker" plumes, and the criterion for buoyancy reversal, *Earth Planet. Sci. Lett.*, *8*6, 85-92,
576 doi:0.1016/0012-821X(87)90191-9.
577
578 Van Ark, E.M., R.S. Detrick, J.P. Canales, S.M. Carbotte, A.J. Harding, G.M. Kent, M.R.
579 Nedimović, W.S.D. Wilcock, J.B. Diebold and J.M Babcock (2007), Seismic structure of the
580 Endeavour Segment, Juan de Fuca Ridge: Correlations with seismicity and hydrothermal
581 activity, *J. Geophys. Res, 112,* B02401, doi:10.1029/2005JB004210.

582

583 Wilcock, S.D., E.E. Hooft, D.R. Toomey, P.R. McGill, A.H. Barclay, D.S. Stakes, and T.M.
584 Ramirez (2009), The role of magma injection in localizing black-smoker activity, *Nat.*
585 *Geosci., 2*, 509-513, doi:10.1038/NGEO0550.

586

587 Wilson, D.J., A.H. Robinson, R.W. Hobbs, C. Peirce, and M.J. Funnell (2019), Does
588 intermediate spreading-rate oceanic crust result from episodic transition between magmatic
589 and magma-dominated, faulting-enhanced spreading? — The Costa Rica Rift example,
590 *Geophys. J. Int.*, *218*, 1617–1641, https://doi.org/10.1093/gji/ggz184.

591

592 Zhang L., V.C.H. Tong, R.W. Hobbs and D.J. Wilson (2016), 3D crustal structure beneath the
593 Costa Rica Rift from seismic tomography: Insight into magmatic activity, *AGU*, Fall
594 Meeting Abstract T22C-02.

595

596 Zhang, L., V.C.H. Tong, R.W. Hobbs, C. Peirce, R. Lowell, G. Haughton, B.J. Murton, M.A.
597 Morales Maqueda and A. Robinson (2017), Axial crustal structure of the Costa Rica Rift:
598 Implications for along-axis hydrothermal circulation, *AGU*, Fall Meeting Abstract T31C-06.

599

600

**Figure Captions**

Figure 1. Swath bathymetry map of the Costa Rica Rift (CRR). Black dashed lines mark the cruise track of JC114 in the vicinity of the CRR axis. Solid black lines show the locations of MCS profiles NG_Bb13, 1268 and NG_G10; red triangles indicate OBS locations; blue and red crosses indicate CTTD cast locations discussed in this study. Inset (top right) shows location of the study area (blue rectangle) in the Panama Basin. Principal bathymetric and tectonic features are labelled: the Cocos Ridge, the Galapagos Islands, the Carnegie Ridge, the Malpelo Ridge, the Ecuador Trench, the Galapagos Spreading Ridge (GSR), the Inca Transform (IT), the Ecuador Rift (ER), the Ecuador Fracture Zone (EFZ), the Costa Rica Rift (CRR), and the Panama Fracture Zone (PFZ). The relative plate motion between the Cocos and Nazca plates is shown (mm/yr) along with the location of the ODP site 504B.

**Figure 2.** Schematic of heat balance model linking axial magma lens heat content to plume heat content showing the relationship of some of the important parameters.

**Figure 3.** (a) CTD/transmissometry (CTTD) casts along Costa Rica Rift axis showing decreased transmissivity between 2500 m to 2800 m depth. Ridge axis is 3150 m depth. Red curve is a mean of seven profiles (black curves); (b) Results from $\Delta^3$He analyses from water samples taken over the CRR at CTTD 6 (09-12-2014, blue points) and CTTD 55 (02-01-2015, red points). Note the elevated value within the depth range of decreased transmissivity. (c) Abyssal stratification over the ridge axis, where $N^2$ is a squared Brunt-Väisälä frequency. Black lines show individual casts. Dotted and solid red lines show averages displaying higher and lower order data trends

624 respectively. Solid horizontal gray line indicates the top of the transmissivity and $\Delta^3$He
625 anomalies, and change in slope of $N^2$, interpreted as representing the top of the plume. Dashed
626 horizontal gray line indicates the base of the transmissivity anomaly.
627
628 **Figure 4.** Seismic reflection images of the axial magma lens (AML) for MCS profiles shown on
629 Figure 1. (a) Line 1268 from the 1994 survey. (b) Line NG_Bb13 and (c) line NG_G10 from the
630 2015 survey. Black dots indicate the AML reflection at ~5.1-5.3 s TWTT. Comparing the
631 stacked image of the AML in (a) with that in (b), we can observe that AML extends westward
632 and its length increases from 2.4 to 6.0 km during the 21 years that separate the surveys.
633 Locations of the non-transform discontinuity (NTD), the intersections between N-S and E-W
634 lines and the average spreading rates over the past 4 My [*Wilson et al.*, 2019] between the Cocos
635 and Nazca plates are labelled.
636
637 **Figure 5.** 1-D five-layer velocity-depth model (a) and its corresponding reflectivity (b) used to
638 forward modelling a CDP gather [after *Wilson et al.,* 2019]. The black line denotes P-wave
639 velocity ($V_p$), the red line S-wave velocity ($V_s$) and the green line density ($\rho$). The solid and
640 dashed blue lines show the OBS and MCS inversion derived 1-D velocity structure at the ridge
641 axis respectively, and the dotted purple line shows the OBS forward modelling 1-D velocity
642 structure (all from *Wilson et al.,* 2019). (c) Synthesized waveforms and (d) observed records of
643 an example CDP gather (1217 from line 1268) with trace offsets incrementing every 25 m and
644 ranging from 187.5 m to 462.5 m. The seabed (water-bottom) and AML reflections are labeled.
645

**Figure 6.** Microseismicity at the CRR. (a) Swath bathymetry of the CRR. Inverted red triangles indicate OBS locations used for picking and relocating earthquake locations. Dots are earthquake hypocenters, colored by elapsed time in Julian days since the start of 2015. Black line shows the location of line NG_Bb13. (b) Depth distributions of hypocenters across the ridge axis. (c) Depth distributions of hypocenters along the ridge axis overlaid on a time-to-depth converted migrated seismic image of line NG_Bb13. The majority of microearthquakes are located directly above the AML. The location of the NTD is labelled.

655 **Table 1. Symbols and parameters**

656

| Symbol | Meaning | Value/Units |
|---|---|---|
| $A_d$ | Area of discharge zone | $m^2$ |
| $A_m$ | Area of AML | $m^2$ |
| $c_p$ | Specific heat of seawater | 4-5 x $10^3$ J $kg^{-1}$ °$C^{-1}$ |
| $c_m$ | Specific heat of magma | 1.1 x $10^3$ J $kg^{-1}$ °$C^{-1}$ |
| $F_0$ | Buoyancy flux | $m^4$ $s^{-3}$ |
| $g$ | Acceleration due to gravity | 9.8 m $s^{-2}$ |
| $H$ | Hydrothermal heat output | Watts |
| $H_m$ | AML heat content | J |
| $k$ | Permeability | $m^2$ |
| $L$ | Latent heat of magma | 4 x $10^5$ J $kg^{-1}$ |
| $N^2$ | Brunt-Väisälä frequency | $s^{-2}$ |
| $Q$ | Volume flux of fluid | $m^3$ $s^{-1}$ |
| $T_m$ | Magma liquidus temperature | 1200°C |
| $T_v$ | Hydrothermal vent temperature | 350°C |
| $V_m$ | Volume of melt | $m^3$ |
| z | Vertical coordinate | |
| $Z^*$ | Maximum plume rise height | m |
| *Greek symbols* | | |
| $\alpha$ | Thermal expansion coefficient of seawater | 1.5 x $10^{-4}$ °$C^{-1}$ |
| $\alpha_d$ | Thermal expansion coefficient of hydrothermal fluid in discharge zone | $10^{-3}$ °$C^{-1}$ |
| $\delta$ | Thermal boundary layer thickness | m |
| $\lambda$ | Thermal conductivity of magma | 2.0 W $m^{-1}$ °$C^{-1}$ |
| $\rho$ | Fluid density | kg $m^{-3}$ |
| $\rho_0$ | Background seawater density | 1000 kg $m^{-3}$ |
| $\rho_m$ | Magma density | 2700 kg $m^{-3}$ |
| $\nu_d$ | Kinematic viscosity of hydrothermal fluid | $10^{-7}$ $m^2$ $s^{-1}$ |

657
658
659

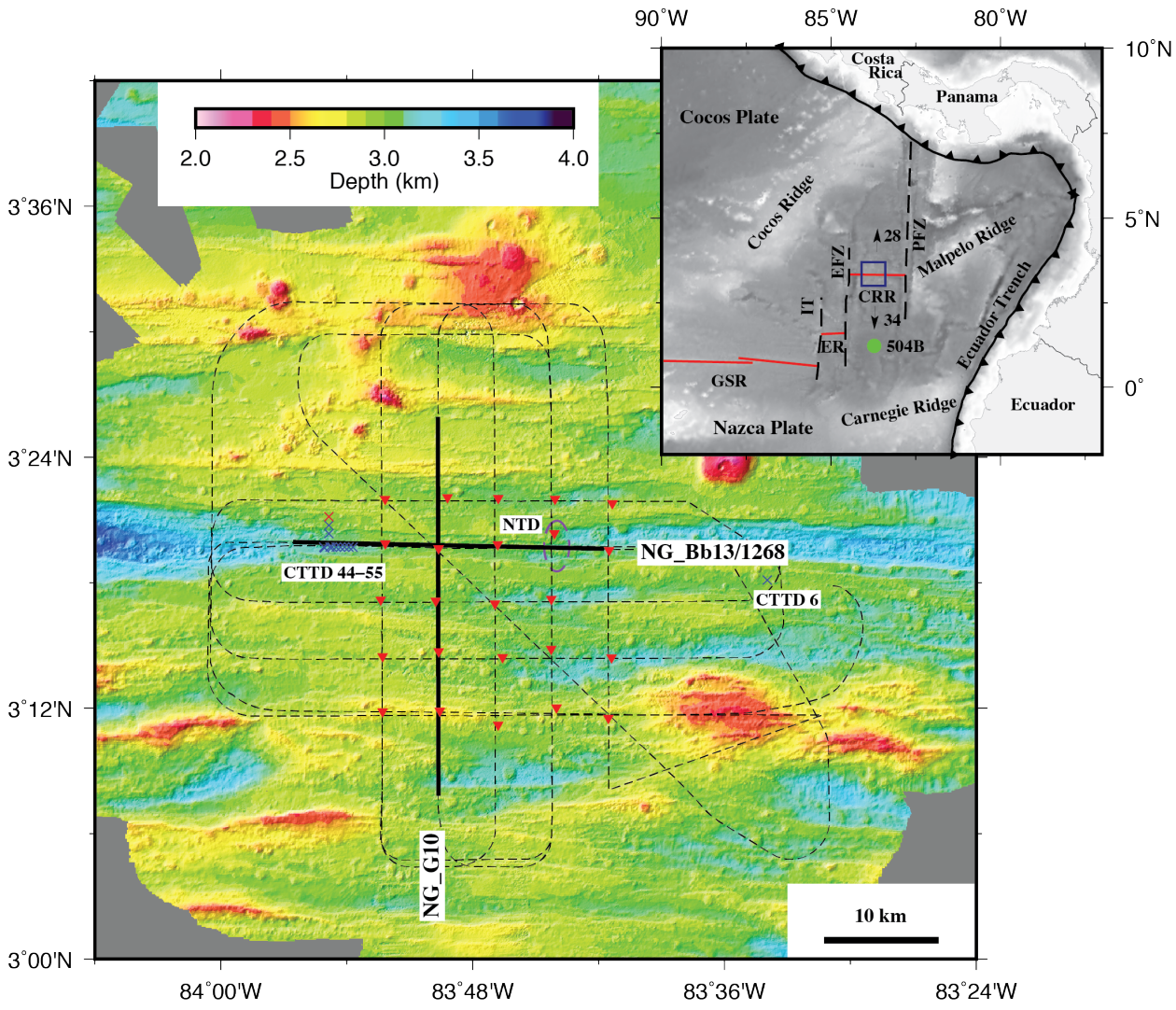
90˚W
85˚W
80˚W
10˚N
5˚N
0˚
3˚36'N
3˚24'N
3˚12'N
3˚00'N
84˚00'W
83˚48'W
83˚36'W
83˚24'W
2.0
2.5
3.0
3.5
4.0
Depth (km)
NTD
NG_Bb13/1268
CTTD 44–55
CTTD 6
NG_G10
10 km
Costa Rica
Panama
Cocos Plate
Cocos Ridge
EFZ
PFZ
28
34
CRR
IT
ER
504B
Malpelo Ridge
Ecuador Trench
GSR
Nazca Plate
Carnegie Ridge
Ecuador

Figure 1.

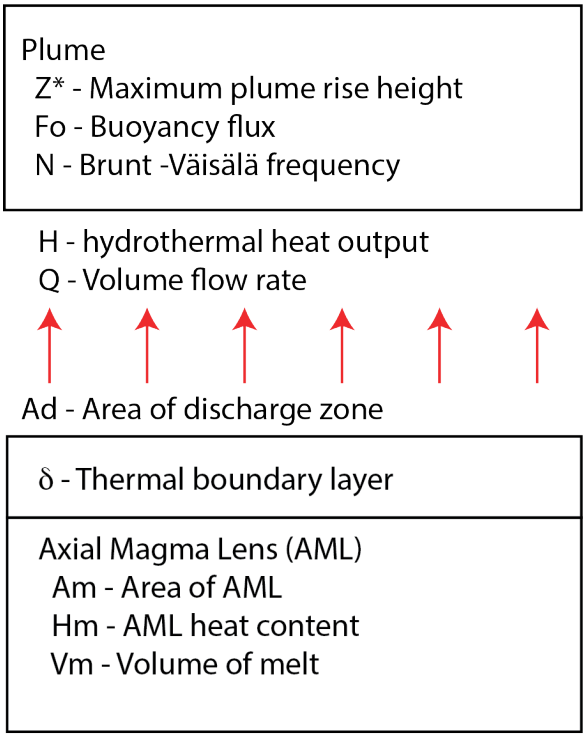


662 Figure 2.
663

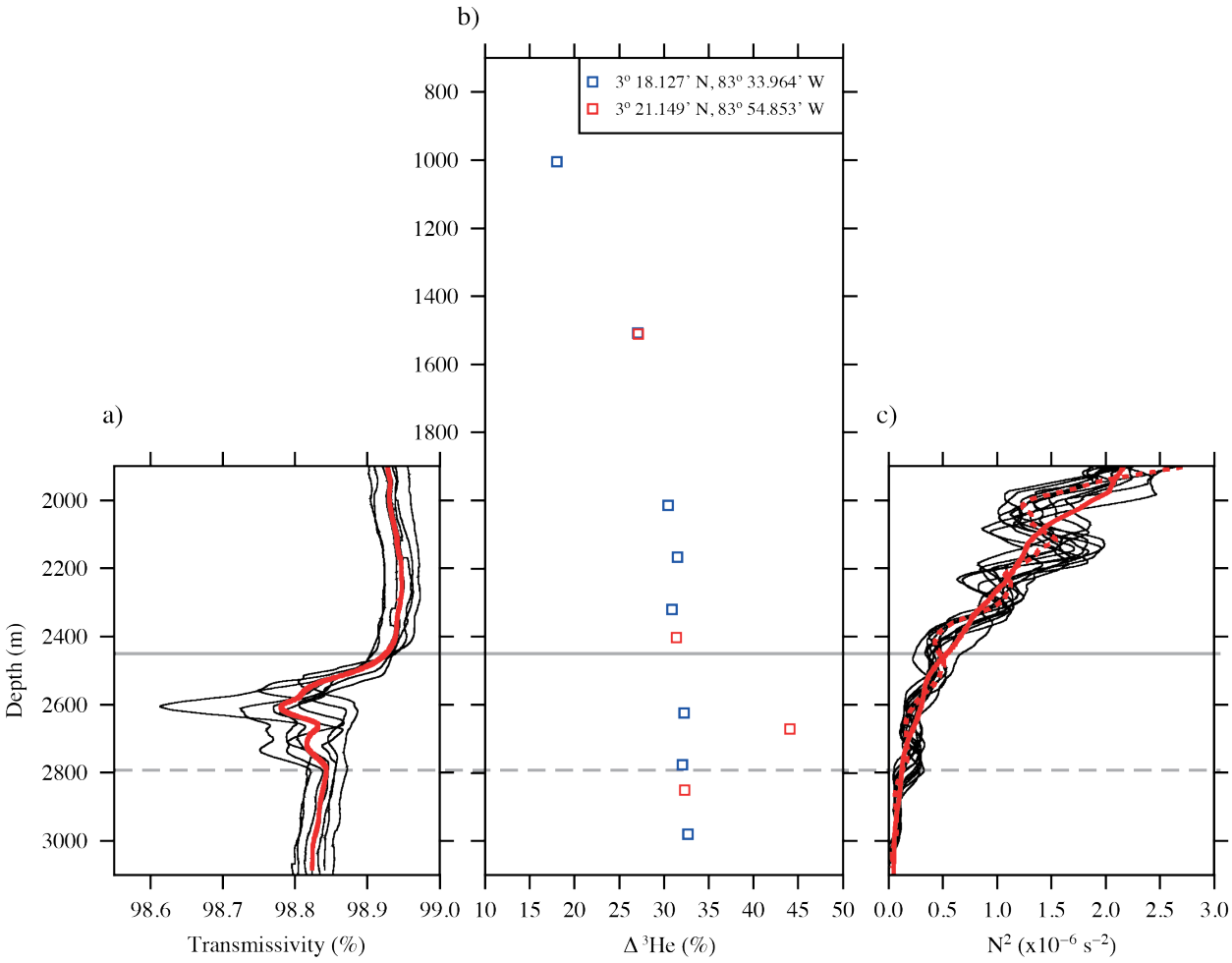
b)
3° 18.127' N, 83° 33.964' W
3° 21.149' N, 83° 54.853' W
800
1000
1200
1400
1600
1800
a)
c)
2000
2200
2400
2600
2800
3000
Depth (m)
98.6
98.7
98.8
98.9
99.0
Transmissivity (%)
10
15
20
25
30
35
40
45
50
Δ ³He (%)
0.0
0.5
1.0
1.5
2.0
2.5
3.0
N² (x10⁻⁶ s⁻²)

664

Figure 3.

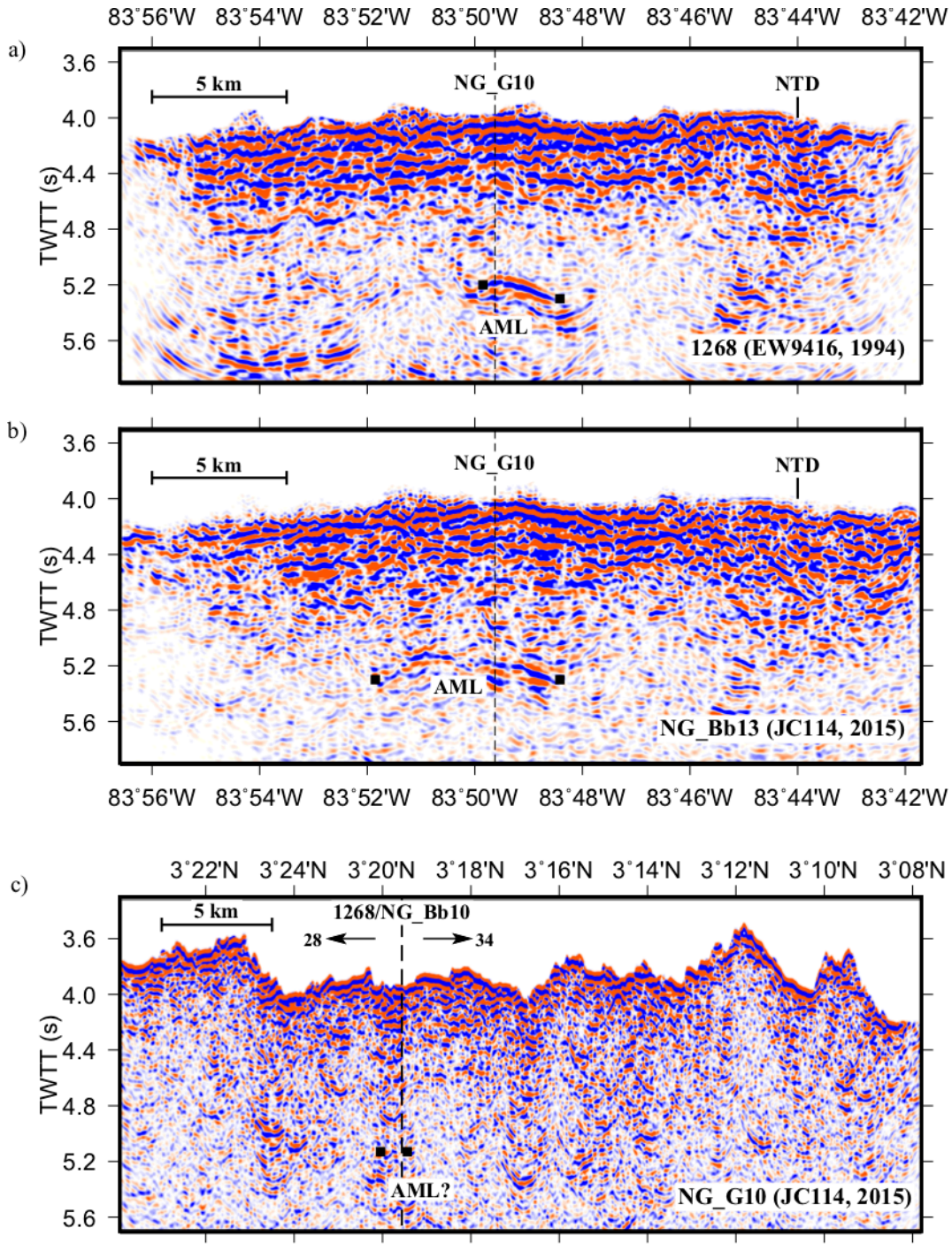
a)
83°56'W 83°54'W 83°52'W 83°50'W 83°48'W 83°46'W 83°44'W 83°42'W
5 km
NG_G10
NTD
TWTT (s)
3.6
4.0
4.4
4.8
5.2
5.6
AML
1268 (EW9416, 1994)
b)
5 km
NG_G10
NTD
AML
NG_Bb13 (JC114, 2015)
83°56'W 83°54'W 83°52'W 83°50'W 83°48'W 83°46'W 83°44'W 83°42'W
c)
3°22'N 3°24'N 3°20'N 3°18'N 3°16'N 3°14'N 3°12'N 3°10'N 3°08'N
5 km
1268/NG_Bb10
28
34
AML?
NG_G10 (JC114, 2015)

665

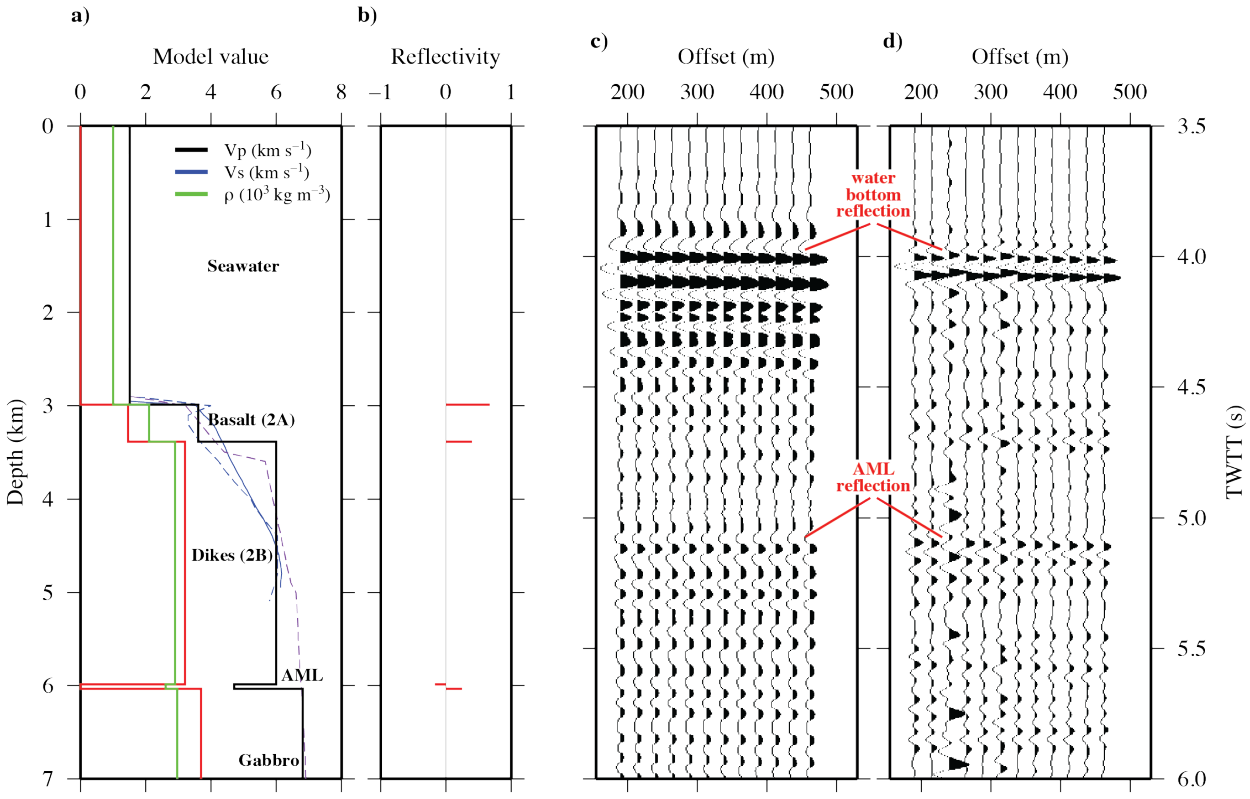
a)
b)
c)
d)
Model value
Reflectivity
Offset (m)
Offset (m)
Vp (km s$^{-1}$)
Vs (km s$^{-1}$)
ρ (10$^3$ kg m$^{-3}$)
Seawater
Basalt (2A)
Dikes (2B)
AML
Gabbro
Depth (km)
water bottom reflection
AML reflection
TWTT (s)

666

Figure 5.

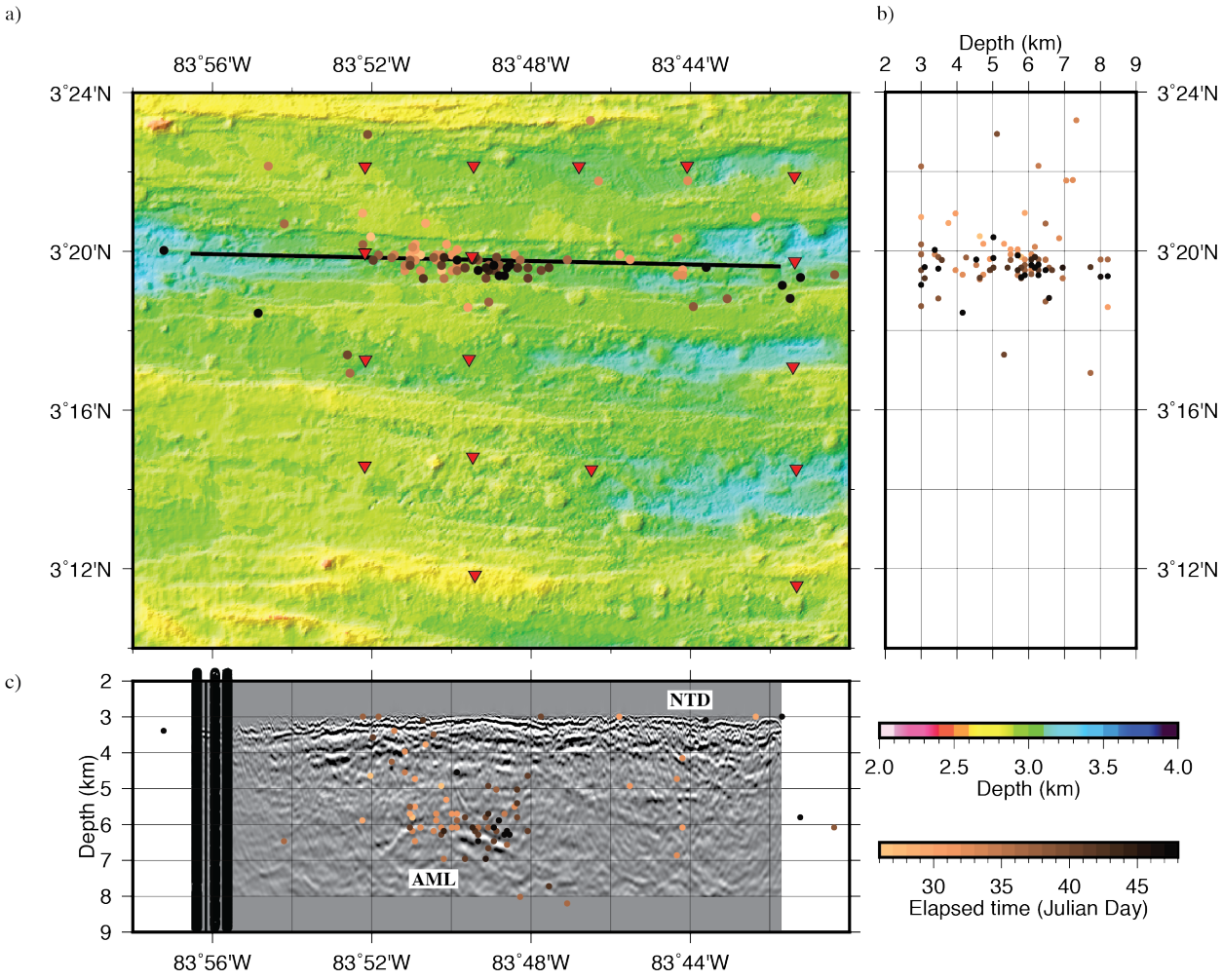
a)
b)
c)
83°56'W
83°52'W
83°48'W
83°44'W
3°24'N
3°20'N
3°16'N
3°12'N
Depth (km)
2 3 4 5 6 7 8 9
NTD
AML
2.0 2.5 3.0 3.5 4.0
Depth (km)
30 35 40 45
Elapsed time (Julian Day)

667

Figure 6.